

# Opto-Valleytronic Spin Injection in Monolayer MoS<sub>2</sub>/Few-Layer Graphene Hybrid Spin Valves

Yunqiu Kelly Luo,<sup>†</sup> Jinsong Xu,<sup>†</sup> Tiancong Zhu,<sup>†</sup> Guanzhong Wu,<sup>†</sup> Elizabeth J. McCormick,<sup>†</sup> Wenbo Zhan,<sup>‡</sup> Mahesh R. Neupane,<sup>‡</sup> and Roland K. Kawakami<sup>\*,†</sup>

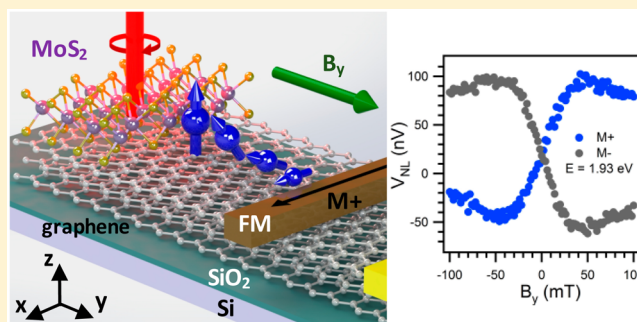
<sup>†</sup>Department of Physics, The Ohio State University, Columbus, Ohio 43210, United States

<sup>‡</sup>Sensors and Electron Devices Directorate, U.S. Army Research Laboratory, Adelphi, Maryland 20783, United States

## S Supporting Information

**ABSTRACT:** Two-dimensional (2D) materials provide a unique platform for spintronics and valleytronics due to the ability to combine vastly different functionalities into one vertically stacked heterostructure, where the strengths of each of the constituent materials can compensate for the weaknesses of the others. Graphene has been demonstrated to be an exceptional material for spin transport at room temperature; however, it lacks a coupling of the spin and optical degrees of freedom. In contrast, spin/valley polarization can be efficiently generated in monolayer transition metal dichalcogenides (TMD) such as MoS<sub>2</sub> via absorption of circularly polarized photons, but lateral spin or valley transport has not been realized at room temperature. In this Letter, we fabricate monolayer MoS<sub>2</sub>/few-layer graphene hybrid spin valves and demonstrate, for the first time, the opto-valleytronic spin injection across a TMD/graphene interface. We observe that the magnitude and direction of spin polarization is controlled by both helicity and photon energy. In addition, Hanle spin precession measurements confirm optical spin injection, spin transport, and electrical detection up to room temperature. Finally, analysis by a one-dimensional drift-diffusion model quantifies the optically injected spin current and the spin transport parameters. Our results demonstrate a 2D spintronic/valleytronic system that achieves optical spin injection and lateral spin transport at room temperature in a single device, which paves the way for multifunctional 2D spintronic devices for memory and logic applications.

**KEYWORDS:** Spintronics, valleytronics, graphene, transition metal dichalcogenides, optoelectronics



Spintronics and valleytronics, novel fields with large potential impacts in both fundamental science and technology, utilize the electron's spin and valley degrees of freedom, in addition to charge, for information storage and logic operations. In the past decade, experimental studies have established single-layer and multilayer graphene as among the most promising materials for spintronics due to their high electronic mobility combined with low intrinsic spin–orbit coupling. Graphene exhibits room-temperature spin diffusion length of up to tens of microns, substantially longer than conventional metals or semiconductors ( $<1 \mu\text{m}$ ).<sup>1–4</sup> However, graphene's lack of spin-dependent optical selection rules has made opto-spintronic functionality impossible, a substantial limitation for graphene.

Fortunately, monolayer MoS<sub>2</sub> and related semiconducting transition metal dichalcogenides (TMDs) exhibit favorable characteristics for nanoscale opto-valleytronic and opto-spintronic applications.<sup>5–7</sup> TMDs have strong spin–orbit coupling due to the heavy metal atom and lack inversion symmetry in monolayer form, the combination of which allows complete simultaneous valley and spin polarization through absorption of circularly polarized light.<sup>8–14</sup> This originates from the valley-dependent optical selection rules of monolayer MoS<sub>2</sub>, where the absorption of circularly polarized  $\sigma^+$  ( $\sigma^-$ ) photons excites electrons only in

the K (K') valley. Because this valley selection rule derives from the symmetries of the lattice, it is a general rule that also applies to systems with low SO coupling such as monolayer hBN and gapped graphene<sup>9,10</sup> where the valley-dependent optical transition is independent of spin. In monolayer MoS<sub>2</sub>, however, the spin selection is induced by the strong SO coupling. In the K (K') valley, the valence band has a large spin–orbit splitting with a spin up (down) state at the valence band maximum and spin down (up) state lower in energy, with an SO splitting of  $\sim 150 \text{ meV}$ .<sup>8,15</sup> Therefore, the spin and valley degrees of freedom are strongly coupled, and the valley optical selection rule can be used to generate spin-polarized photoexcitation.

The true strength of graphene and TMDs for spin- and valleytronics lies in the combination of the two materials, where the strengths of each material can compensate for the weaknesses of the other. It has already been demonstrated that manipulation of spin currents in graphene is possible through proximity to TMDs via spin absorption,<sup>16,17</sup> as well as the

**Received:** April 4, 2017

**Revised:** May 15, 2017

**Published:** May 23, 2017



proximity to magnetic insulators through exchange fields.<sup>18,19</sup> Additionally, Fabian and co-workers proposed that the absorption of circularly polarized photons in monolayer MoS<sub>2</sub> will create valley/spin polarized excitations that can generate spin injection into an adjacent graphene layer.<sup>20</sup> This would provide a route toward opto-spintronic functionality in graphene by creating a vertical heterostructure with monolayer MoS<sub>2</sub>.

In this Letter, we experimentally demonstrate spin injection from monolayer MoS<sub>2</sub> to few-layer graphene following optical valley/spin excitation in MoS<sub>2</sub> with circularly polarized light. We detect spins in graphene through voltage signals on a ferromagnetic (FM) electrode in a nonlocal measurement geometry. Notably, the spins in graphene precess in an external magnetic field, and we obtain antisymmetric Hanle spin precession curves, which prove that the measured voltage signals originate from optical spin injection and spin transport. In addition, we find that tuning the photon energy adjusts the magnitude and direction of the injected spin polarization, which is a direct consequence of the large spin splitting in the valence band of MoS<sub>2</sub>. Low-temperature measurements (10 K) reveal a double peak structure in the spin signal spectrum near the A exciton resonance, while measurements at elevated temperatures find that the opto-valleytronic spin injection into graphene persists up to room temperature. Lastly, we quantify the injected spin current using a one-dimensional spin transport model based on the Bloch equations. Our results demonstrate unprecedented spintronic/valleytronic functionality of a TMD/graphene device by integrating opto-valleytronic spin injection, lateral spin transport, and electrical spin detection in a single van der Waals heterostructure.

As illustrated in Figure 1, the concept of the experiment is to optically excite spin/valley polarization in MoS<sub>2</sub> in order to

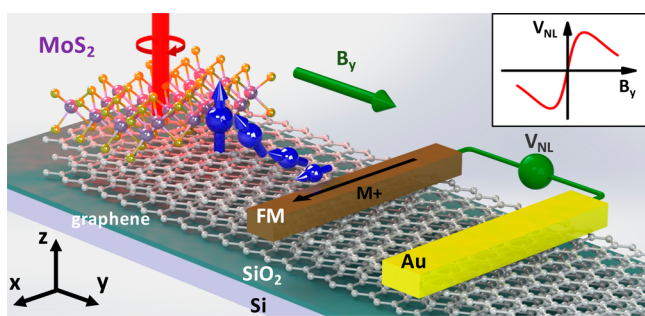


**Figure 1.** Illustration of optical spin injection, lateral spin transport, and electrical spin detection in a monolayer MoS<sub>2</sub>/few-layer graphene hybrid spin valve structure. Inset: expected signal  $V_{NL}$  as a function of applied magnetic field  $B_y$ .

inject spin polarization into the underlying graphene, where it diffuses and precesses in an external magnetic field, and is finally detected electrically by a FM electrode. We begin with the absorption of circularly polarized photons in monolayer MoS<sub>2</sub> to produce spin/valley-polarized carriers oriented out-of-plane (along + $z$ ), which subsequently transfer into the adjacent few-layer graphene. The spins (blue arrows) then diffuse within the few-layer graphene toward a ferromagnetic (FM) spin detector with in-plane magnetization. To detect the spin transport, a magnetic field  $B_y$  is applied to induce spin precession. This generates a nonzero component of spin-polarization ( $S_x$ ) along the FM detector's magnetization, which produces a detector voltage ( $V_{NL}$ ) that is proportional to  $S_x$ . By measuring  $V_{NL}$  as a

function of  $B_y$ , the combined processes of optical spin injection, lateral spin transport, and electrical spin detection can be identified as an antisymmetric Hanle curve as shown schematically in the Figure 1 inset.

To realize this experimentally, we fabricate a monolayer MoS<sub>2</sub>/few-layer graphene hybrid spin valve, shown in Figure 2a. This device consists of n-type few-layer graphene (black dashed lines) contacted by monolayer MoS<sub>2</sub> (red dashed lines), Cr/Au electrodes (G1, G2), and Co electrodes with SrO tunnel barriers (C1–C10). Details of sample fabrication and material characterization are in the Supporting Information (SI), Sec. 1. Before attempting optical spin injection, we first establish the proper electrical spin injection, transport, and detection processes in few-layer graphene using the nonlocal magnetotransport geometry at 10 K, as shown in Figure 2b. The current  $I_{inj}$  ( $= 1 \mu A$ ) injects spin polarized electrons into graphene at injector electrode C6. The spins subsequently diffuse in graphene toward the spin detector C8, where it is measured as a voltage signal  $V_{NL}$  across electrodes C8 and G2 (nonmagnetic reference electrode). Figure 2c shows  $V_{NL}$  as a function of magnetic field applied parallel to the Co electrodes ( $B_x$ ), resulting in hysteretic jumps as the Co magnetizations switch between parallel (high  $V_{NL}$ ) and antiparallel (low  $V_{NL}$ ) configurations. The presence of these jumps in  $V_{NL}$  indicates spin transport through graphene. To extract the spin transport parameters of the few-layer graphene, we perform in-plane Hanle spin precession measurements by applying a magnetic field perpendicular to the electrode axis ( $B_y$ ). The measured  $V_{NL}$  for parallel (red circles in Figure 2d) and antiparallel (blue circles in Figure 2d) states are analyzed to yield a spin lifetime of  $\tau_G = 308$  ps, diffusion coefficient  $D_G = 0.0301$  m<sup>2</sup>/s, and spin diffusion length of  $\lambda_G = \sqrt{D_G \tau_G} = 3.04 \mu m$  (see SI, Section 2 for details of the spin transport measurement and analysis).

Next, we determine the appropriate photon energy for optical spin injection into MoS<sub>2</sub> by performing optical reflection spectroscopy and photocurrent spectroscopy of the MoS<sub>2</sub>/graphene heterostructure at 10 K. A focused beam ( $\sim 2 \mu m$ , 100  $\mu W$ ) from a tunable laser is incident on the MoS<sub>2</sub>/graphene heterostructure, and the reflection contrast  $\Delta R/R$  (compared to the substrate) is measured as a function of incident photon energy. At the same time, the photocurrent response ( $I_{ph}$ ) is measured across electrodes G1 and G2. The reflection contrast spectrum (Figure 3a) shows the maximum contrast at  $\sim 1.93$  eV and  $\sim 2.06$  eV, which correspond to the A and B exciton resonances of monolayer MoS<sub>2</sub>.<sup>6,12,15,21</sup> Similarly, we observe two peaks at nearly identical photon energies in the photocurrent spectrum (Figure 3b) (see SI, Section 3 for details of the measurements).

Having established the optimal energy for light absorption and the ability to detect spins electrically, we turn our attention to the combined functionality of optical spin injection and lateral spin transport in the MoS<sub>2</sub>/graphene hybrid spin valve. As illustrated in Figure 3c, we focus the laser beam ( $\sim 2 \mu m$ , 100  $\mu W$ ) on the MoS<sub>2</sub>/graphene junction at a photon energy of 1.93 eV (A exciton) for the optical spin injection and measure the voltage  $V_{NL}$  across electrodes C6 and G2 for electrical spin detection. We also magnetize the detector electrode magnetization along + $x$  direction (denoted as M+). Circular polarization of the incident light produces spin/valley polarization in the MoS<sub>2</sub> layer with spin oriented out-of-plane (for noise rejection, we modulate the helicity and detect using lock-in techniques, as discussed in the SI, Section 4). A coherent

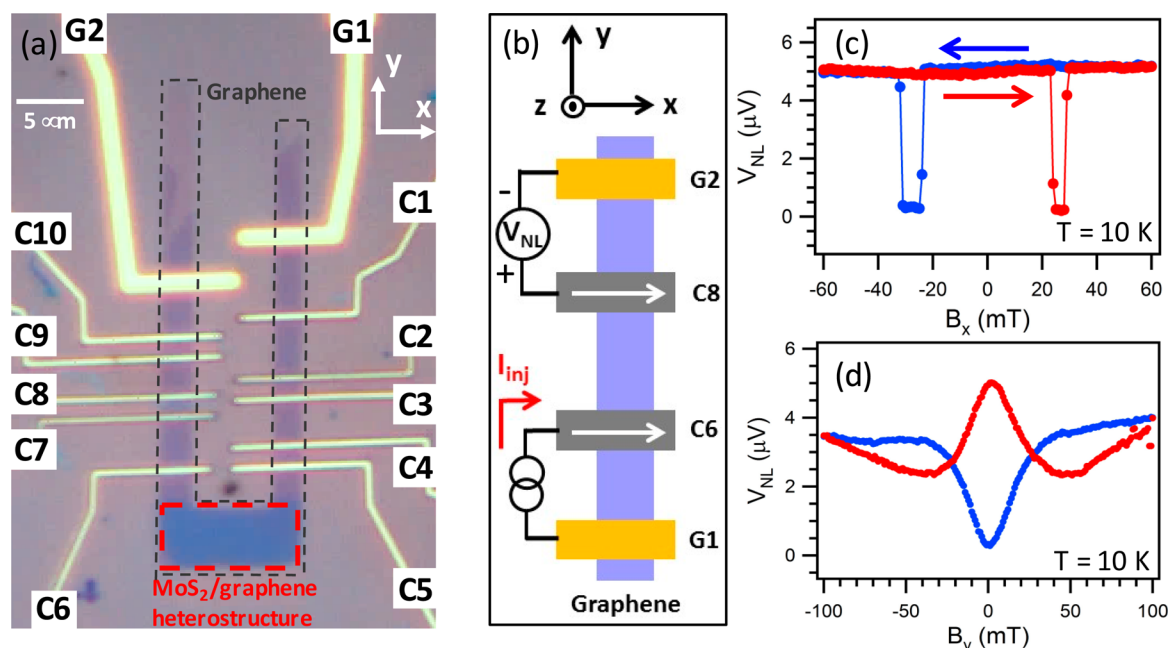


**Figure 2.** Electrical spin transport measurements in few-layer graphene. (a) Optical microscope image of a monolayer MoS<sub>2</sub>/few-layer graphene hybrid spin valve. The black dashed line highlights the few-layer graphene region. The red dashed line highlights the monolayer MoS<sub>2</sub>/graphene junction region. C1–10 are cobalt electrodes. G1 and G2 are gold electrodes. (b) Schematic of the nonlocal spin valve measurement. (c) Nonlocal spin valve measurement. The red (blue) curve is for the up (down) sweep of magnetic field  $B_x$  parallel to the Co magnetization. (d) In-plane Hanle spin precession measurement. The red (blue) curve is for the parallel (antiparallel) alignment of the Co magnetizations.

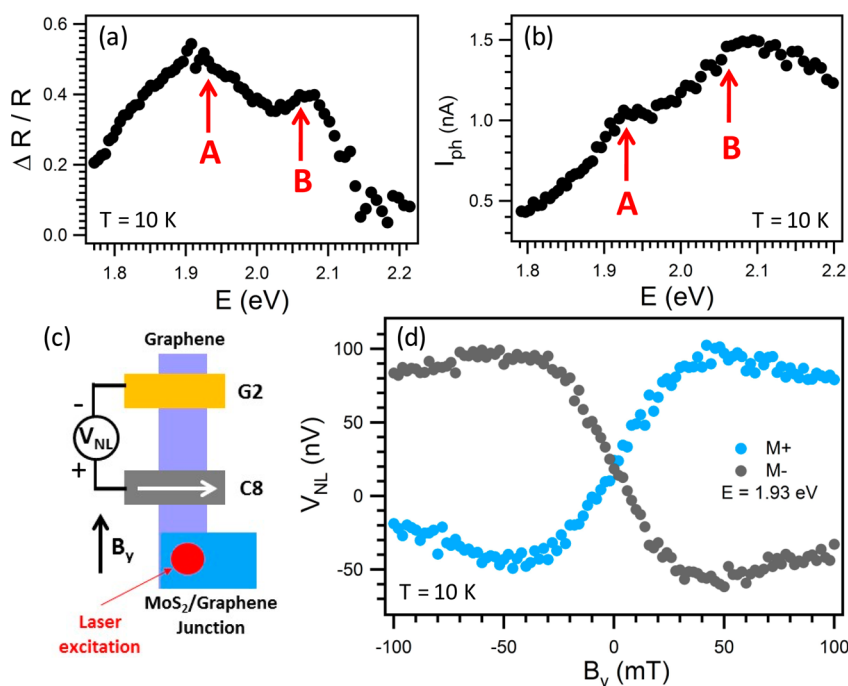


**Figure 3.** Electrical spin detection of the opto-valleytronic spin injection. (a) Reflection contrast spectrum of monolayer MoS<sub>2</sub>/few-layer graphene relative to the SiO<sub>2</sub>/Si substrate. The arrows indicate contrast peaks at the A and B exciton resonances. (b) Dependence of junction photocurrent on photon energy. The arrows indicate the A and B exciton resonances. (c) Schematic of the opto-valleytronic spin injection experiment. (d) Electrical spin signal  $V_{NL}$  as a function of  $B_y$  exhibits clear antisymmetric Hanle spin precession signals which flip polarity with the Co magnetization direction (M+ vs M−). The photon energy is tuned to the A exciton resonance at  $E = 1.93$  eV.

transfer of spin across the MoS<sub>2</sub>/graphene interface results in out-of-plane spin polarization in the graphene layer, which will subsequently diffuse toward the FM detector (C6). Because the spin orientation is perpendicular to the detector magnetization, this will result in zero spin signal in  $V_{NL}$ . To detect spins,

we therefore apply an external in-plane field ( $B_y$ ) along the graphene strip to induce spin precession and generate a component of spin along the detector magnetization (+ $x$  direction). The light blue curve in Figure 3d shows the measured voltage  $V_{NL}$  as a function of  $B_y$ . At low fields,  $V_{NL}$  varies approximately



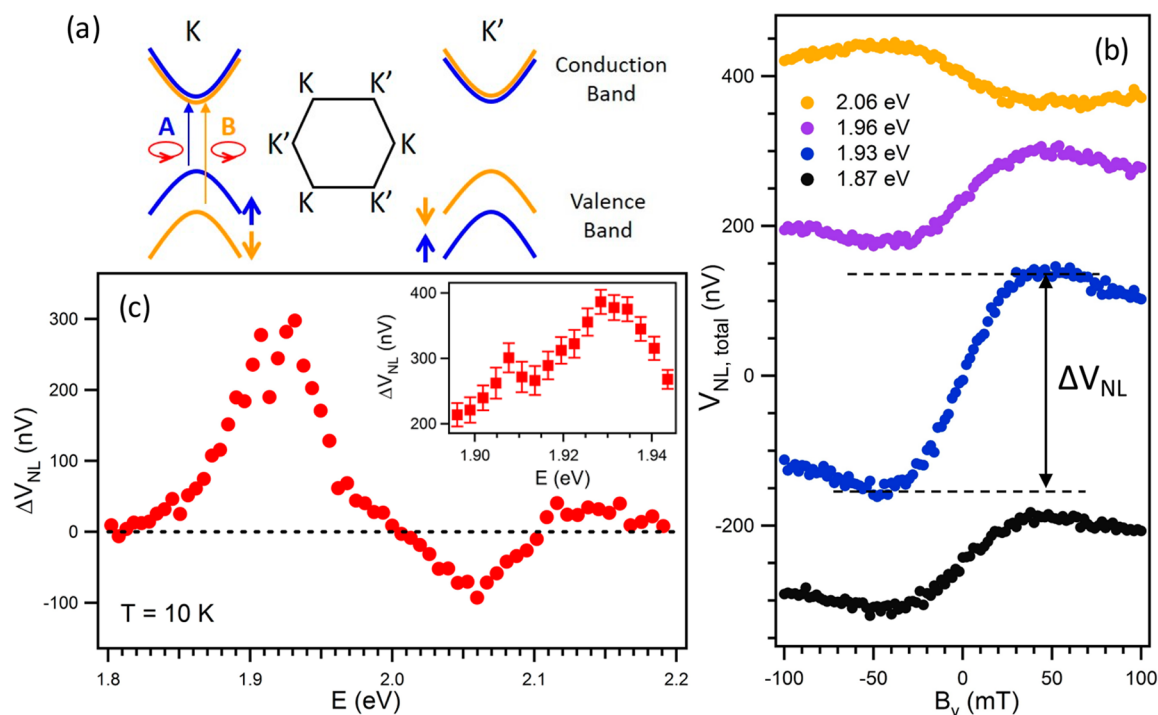


**Figure 4.** Photon energy dependence of opto-valleytronic spin injection. (a) Schematic band structure of monolayer MoS<sub>2</sub> at the K and K' valleys. (b) Representative antisymmetric Hanle curves at four photon energies (1.87, 1.93, 1.96, and 2.06 eV). (c) Spin signal  $\Delta V_{NL}$  as a function of photon energy. Inset shows zoom-in detailed features around the A exciton resonance.

linearly with  $B_y$ , because the spin precession angle varies linearly with the field. At higher fields, the increase of  $V_{NL}$  with  $B_y$  eventually reaches a maximum and reduces as the average precession angle exceeds  $\sim 90^\circ$ . Later, we provide a quantitative description of this curve, known as an “antisymmetric Hanle curve”, by modeling the spin transport and precession using one-dimensional drift-diffusion equations. To verify that the signal indeed comes from spin, we reverse the FM magnetization direction (M $\rightarrow$ ) and repeat the measurement. The result is an inverted  $V_{NL}$  signal, as shown in the dark gray curve of Figure 3d, which is the expected behavior for a  $V_{NL}$  signal generated by spin polarization. The observation of antisymmetric Hanle curves that flip with the magnetization state (M $\rightarrow$  vs M $\leftarrow$ ) provides proof of optical spin injection into MoS<sub>2</sub>, followed by coherent spin transfer across the MoS<sub>2</sub>/graphene interface, lateral spin transport in graphene, and electrical spin detection. Additional measurements show that the spin transfer from MoS<sub>2</sub> to graphene is dominated by hole transport (SI, Section 5).

Tuning the photon energy from the A exciton to the B exciton should switch the orientation of the injected spin polarization due to the large spin–orbit splitting in the monolayer TMD band structure. As shown in Figure 4a, the valence band of monolayer MoS<sub>2</sub> has a large spin splitting with opposite spin orientation for the A and B optical excitations within the same valley. Figure 4b shows antisymmetric Hanle curves for four different photon energies: 1.87, 1.93, 1.96, and 2.06 eV. At each photon energy,  $V_{NL}$  vs  $B_y$  is measured for both FM magnetization directions (M $\rightarrow$  and M $\leftarrow$ ), and we plot the subtracted signal  $V_{NL, total} = V_{NL, M\rightarrow} - V_{NL, M\leftarrow}$  which helps cancel background signals unrelated to spin. For the A exciton resonance energy (1.93 eV),  $V_{NL, total}$  has a minimum value near  $B_y = -50$  mT and increases to a maximum signal at around  $B_y = 50$  mT. As indicated in Figure 4b, we define the spin signal

as  $\Delta V_{NL} = V_{NL, total}(B_y = 50 \text{ mT}) - V_{NL, total}(B_y = -50 \text{ mT})$ . Away from the A exciton resonance, the Hanle curves for 1.87 eV (black) and 1.96 eV (purple) have smaller spin signals  $\Delta V_{NL}$  than on resonance. In contrast, near the B resonance (2.06 eV), the spin signal completely reverses sign to give a flipped antisymmetric Hanle curve. This indicates a reversal of spin orientation as the photon energy is tuned from the A resonance to the B resonance.

To further investigate the role of photon energy, we map out the detailed photon energy dependence of the spin signal  $\Delta V_{NL}$  at 10 K. We obtain  $\Delta V_{NL}$  at each photon energy by measuring  $V_{NL, total}$  at +50 and  $-50$  mT and plot the resulting  $\Delta V_{NL}$  vs photon energy in Figure 4c. Starting from low photon energy,  $\Delta V_{NL}$  reaches a maximum positive signal near the A resonance (1.90–1.95 eV) and then decreases with increasing photon energy until  $\Delta V_{NL}$  flips sign around 2 eV.  $\Delta V_{NL}$  reaches a minimum near the B resonance at  $\sim 2.06$  eV. This photon energy dependence clearly reflects the nondegenerate spin-split structure of the valence band, which results from strong spin–orbit coupling and the broken inversion symmetry of the monolayer MoS<sub>2</sub> lattice. In the vicinity of the A resonance, we observe a double peak feature. To exclude potential artifacts from noise or sample drift, we retake the data with smaller energy steps and perform a spatial mapping of the spin signal  $\Delta V_{NL}$  over the MoS<sub>2</sub>/graphene junction at each energy (details in SI, Section 6). The inset of Figure 4c plots the maximum  $\Delta V_{NL}$  from the spatial map as a function of photon energy. The presence of two separate peaks near the A resonance can be clearly distinguished. The two peaks are at 1.91 eV and 1.93–1.94 eV, corresponding to a splitting of 20–30 meV. This is consistent with the double peak structure of the A $^-$  trion and A exciton, which exhibits a splitting of 20–40 meV in photoluminescence and optical absorption measurements.<sup>15,22,23</sup>

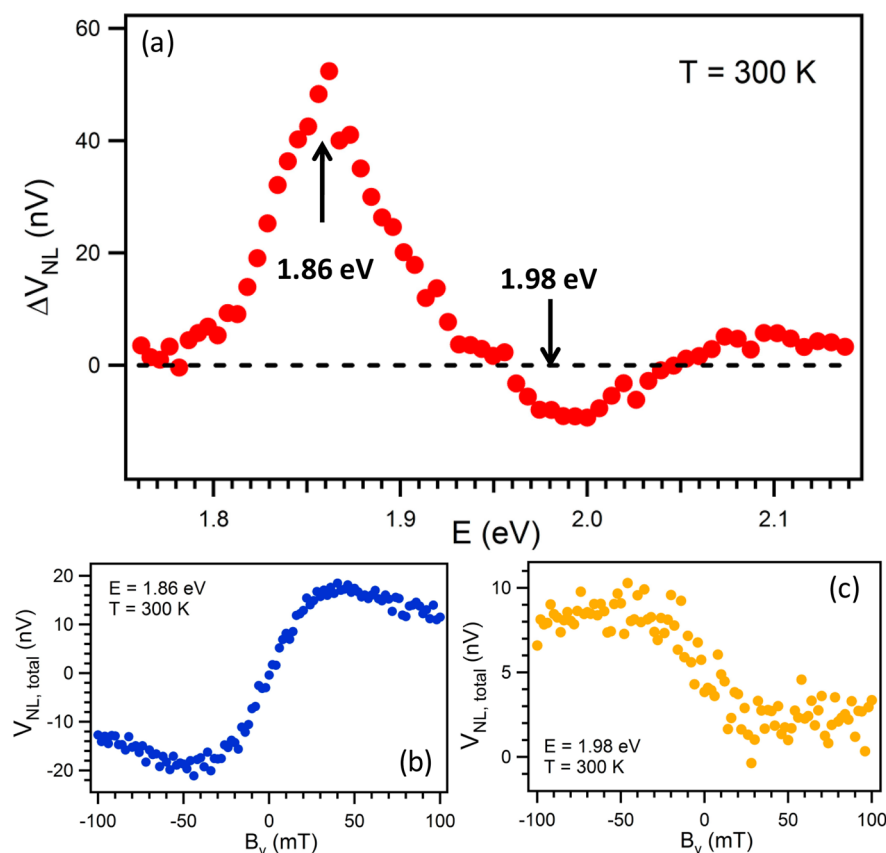


**Figure 5.** Room-temperature characteristics of opto-valleytronic spin injection. (a) Photon energy dependence of the spin signal  $\Delta V_{NL}$ . (b) Antisymmetric Hanle curve at the A resonance (photon energy of 1.86 eV). (c) Antisymmetric Hanle curve at the B resonance (photon energy of 1.98 eV).

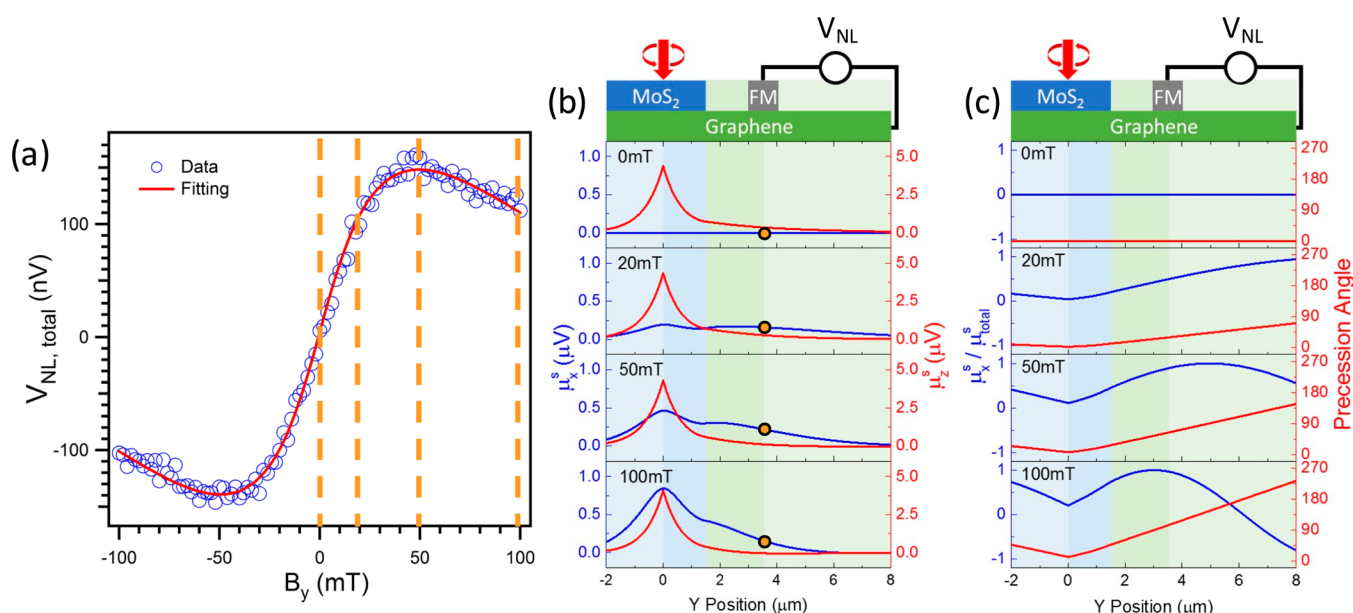


**Figure 6.** Modeling the antisymmetric Hanle curve. (a) Data (open circles) and fitting (red curve) of the antisymmetric Hanle curve for photon energy of 1.93 eV and temperature of 10 K. (b) The  $x$ - and  $z$ -components of spin accumulation in the few-layer graphene as a function of position. The orange circles represent the component of spin accumulation ( $\mu_x^s$ ) measured by the nonlocal voltage  $V_{NL}$ . (c)  $\mu_x^s/\mu_z^s$  and the average precession angle as a function of position.

In addition, we explore the temperatures at which the opto-spintronic device can successfully operate. Remarkably, the signal persists up to room temperature. As shown in Figure 5a,  $\Delta V_{NL}$  at room temperature exhibits a similar dependence on

photon energy as at low temperature, with the positive peak at the A resonance red-shifted to around 1.86 eV, and the negative peak at the B resonance red-shifted to around 1.99 eV. The red shift and peak positions at room temperature are consistent

with previous experimental and theoretical studies.<sup>24,25</sup> Two Hanle scans with photon energies near the A and B peaks are measured (Figure 5b and c) to confirm room temperature spin orientation switching from the A resonance to the B resonance. The room temperature signal is about 5 times smaller than at 10 K. We consider various factors that can give rise to the reduced spin signal at room temperature. In standard graphene spin valves, the spin lifetime and spin diffusion length have a weak temperature dependence,<sup>26</sup> so the graphene alone could not explain the strong temperature dependence that we observe. However, the spin and valley dependent properties in MoS<sub>2</sub> are strongly degraded with increasing temperature. As the temperature increases, there is more intervalley scattering which reduces the valley polarization.<sup>13,27–30</sup> In addition, the spin lifetimes of resident carriers in MoS<sub>2</sub> are also strongly reduced with increasing temperature.<sup>31,32</sup> Thus, the presence of spin signal at room temperature suggests a rapid transfer of spin-polarized carriers from MoS<sub>2</sub> to graphene. Despite the smaller signal, a successful room temperature operation lays the foundation for multifunctional opto-spintronic and opto-valleytronic devices in 2D materials and heterostructures. The data have been reproduced on a second sample (SI, Section 8), and we observe similar effects in preliminary measurements on monolayer MoS<sub>2</sub>/monolayer graphene samples.

To better understand the data and quantify the optical spin injection current, we have developed a one-dimensional model to describe spin transport in the monolayer MoS<sub>2</sub>/few-layer graphene hybrid spin valve. In our model, spin accumulation is considered as a three-component vector ( $\mu_x^s, \mu_y^s, \mu_z^s$ ), where each component describes the spin polarization in different directions. The optically injected spin current from MoS<sub>2</sub> to graphene is modeled as a point source at the center of the laser spot, and we assume that the MoS<sub>2</sub>/graphene and pure graphene regions have different spin transport parameters due to the additional spin relaxation induced by the MoS<sub>2</sub>. In addition, the MoS<sub>2</sub> could generate proximity-induced spin–orbit coupling in the graphene.<sup>20,33,34</sup> However, such effects are not apparent in our data and therefore not incorporated in our model. The lateral spin transport and spin precession are modeled using the steady-state Bloch equation. Details of the model are provided in the SI, Section 9, with Figure 6a showing the best fit to the experimental data taken from Figure 4b (1.93 eV curve). The spin lifetime  $\tau_G = 308$  ps and spin diffusion coefficient  $D_G = 0.0301$  m<sup>2</sup>/s from the electrical nonlocal Hanle measurements (Figure 2d) are used as fixed parameters for the pure graphene region, while  $\tau_M$  and  $D_M$  for the MoS<sub>2</sub>/graphene region are fitting parameters. The best fit yields  $\tau_M = 23.9$  ps and  $D_M = 0.0183$  m<sup>2</sup>/s in the MoS<sub>2</sub>/graphene region and an optically injected spin current of 116 nA.

The corresponding spatial profiles of the spin accumulation components  $\mu_x^s$  and  $\mu_z^s$  are shown in Figure 6b for representative fields  $B_y = 0$  mT, 20 mT, 50 mT, and 100 mT. Because the magnetization of the spin detector is along the  $x$ -axis, the measured signal is proportional to  $\mu_x^s$  at  $y = L$  (detector position) as indicated by the orange circles in Figure 6b. For  $B_y = 0$  mT, the spin population in the channel diffuses without precession. Thus,  $\mu_x^s = 0$  is zero throughout the channel, leading to  $V_{NL} = 0$  at the detector. As the magnetic field is turned on, the spins start to precess while diffusing, and the  $x$ -component of spin accumulation begins to build up in the channel. At  $B_y = 50$  mT, the  $x$  component of spin accumulation underneath the contact reaches a maximum, which results in a maximum nonlocal voltage in Figure 6a. The spin precession is

best illustrated through the spatial profiles of  $\mu_x^s/\mu_{\text{total}}^s$  which is the unit vector of spin accumulation projected along the detector magnetization, as shown in Figure 6c. The average precession angle is given as  $\arctan(\mu_x^s/\mu_{\text{total}}^s)$ . With increasing magnetic field, the precession angle vs position increases in slope as expected, and the position for maximum  $\mu_x^s/\mu_{\text{total}}^s$  moves to the left, closer to the source point. As this maxima passes by the detector, any further increase of  $B_y$  leads to a reduced spin signal, which explains why the antisymmetric Hanle curve in Figure 6a decreases for  $B_y > 50$  mT.

In conclusion, we demonstrate opto-valleytronic spin injection in monolayer MoS<sub>2</sub>/few-layer graphene hybrid spin valves through Hanle spin precession measurements. The magnitude and direction of optically injected spins are tunable by both helicity and photon energy, and the observed spin signals persist up to room temperature. In terms of scaling, such opto-spintronic devices would be subject to the diffraction limit ( $\sim 500$  nm), although the use of near-field optics could allow for smaller devices. These results pave the way for multifunctional 2D spintronic/valleytronic devices and applications.

## ■ ASSOCIATED CONTENT

### ● Supporting Information

The Supporting Information is available free of charge on the ACS Publications website at DOI: 10.1021/acs.nanolett.7b01393.

A description of monolayer MoS<sub>2</sub>/few-layer graphene hybrid spin valve device fabrication, graphene spin transport measurement and analysis, optical reflection and photocurrent spectroscopy (charge currents), experimental setup for the optical injection and electrical detection of spin currents, identifying the carrier type for opto-valleytronic spin injection, spatial mapping of the spin signal, additional measurements, and details of the modeling (PDF)

## ■ AUTHOR INFORMATION

### Corresponding Author

\*E-mail: kawakami.15@osu.edu. Address: 191 W. Woodruff Ave., Department of Physics, The Ohio State University, Columbus, OH 43210. Phone: (614) 292-2515. Fax: (614) 292-7557.

### ORCID

Roland K. Kawakami: 0000-0003-0245-9192

### Author Contributions

Y.K.L. and J.X. contributed equally. R.K.K. conceived the project. Y.K.L. and J.X. fabricated the devices and performed the measurements. G.W., E.J.M., and W.Z. assisted in the measurements. T.Z. and M.R.N. contributed to the modeling and theoretical analysis. All authors contributed to writing the manuscript.

### Notes

The authors declare no competing financial interest.

## ■ ACKNOWLEDGMENTS

We acknowledge helpful discussions with Vladimir Falko and technical assistance from Jyoti Katoch and Simranjeet Singh. This work was primarily supported by NSF DMR-1310661 (optical measurements). We acknowledge partial support from the Center for Emergent Materials: an NSF MRSEC under award number DMR-1420451 (sample fabrication).

## ■ REFERENCES

- (1) Han, W.; Kawakami, R. K.; Gmitra, M.; Fabian, J. *Nat. Nanotechnol.* **2014**, *9*, 794–807.
- (2) Guimarães, M.; Zomer, P.; Ingla-Aynés, J.; Brant, J.; Tombros, N.; van Wees, B. J. *Phys. Rev. Lett.* **2014**, *113*, 086602.
- (3) Drögeler, M.; Franzen, C.; Volmer, F.; Pohlmann, T.; Banszerus, L.; Wolter, M.; Watanabe, K.; Taniguchi, T.; Stampfer, C.; Beschoten, B. *Nano Lett.* **2016**, *16*, 3533–3539.
- (4) Ingla-Aynés, J.; Meijerink, R. J.; van Wees, B. J. *Nano Lett.* **2016**, *16*, 4825–4830.
- (5) Splendiani, A.; Sun, L.; Zhang, Y.; Li, T.; Kim, J.; Chim, C.-Y.; Galli, G.; Wang, F. *Nano Lett.* **2010**, *10*, 1271–1275.
- (6) Mak, K. F.; Lee, C.; Hone, J.; Shan, J.; Heinz, T. F. *Phys. Rev. Lett.* **2010**, *105*, 136805.
- (7) Xu, X.; Yao, W.; Xiao, D.; Heinz, T. F. *Nat. Phys.* **2014**, *10*, 343–350.
- (8) Zhu, Z.; Cheng, Y.; Schwingenschlögl, U. *Phys. Rev. B: Condens. Matter Mater. Phys.* **2011**, *84*, 153402.
- (9) Xiao, D.; Yao, W.; Niu, Q. *Phys. Rev. Lett.* **2007**, *99*, 236809.
- (10) Yao, W.; Xiao, D.; Niu, Q. *Phys. Rev. B: Condens. Matter Mater. Phys.* **2008**, *77*, 235406.
- (11) Xiao, D.; Liu, G.-B.; Feng, W.; Xu, X.; Yao, W. *Phys. Rev. Lett.* **2012**, *108*, 196802.
- (12) Mak, K. F.; He, K.; Shan, J.; Heinz, T. F. *Nat. Nanotechnol.* **2012**, *7*, 494–498.
- (13) Zeng, H.; Dai, J.; Yao, W.; Xiao, D.; Cui, X. *Nat. Nanotechnol.* **2012**, *7*, 490–493.
- (14) Cao, T.; Wang, G.; Han, W.; Ye, H.; Zhu, C.; Shi, J.; Niu, Q.; Tan, P.; Wang, E.; Liu, B. *Nat. Commun.* **2012**, *3*, 887.
- (15) Mak, K. F.; He, K.; Lee, C.; Lee, G. H.; Hone, J.; Heinz, T. F.; Shan, J. *Nat. Mater.* **2012**, *12*, 207–211.
- (16) Yan, W.; Txoperena, O.; Llopis, R.; Dery, H.; Hueso, L. E.; Casanova, F. *Nat. Commun.* **2016**, *7*, 13372.
- (17) Dankert, A.; Dash, S. P. *arXiv:1610.06326*, 2016.
- (18) Leutenantsmeyer, J. C.; Kaverzin, A. A.; Wojtaszek, M.; van Wees, B. J. *2D Mater.* **2017**, *4*, 014001.
- (19) Singh, S.; Katoch, J.; Zhu, T.; Meng, K.-Y.; Liu, T.; Brangham, J. T.; Yang, F. Y.; Flatté, M.; Kawakami, R. K. *Phys. Rev. Lett.* **2017**, *118*, 187201.
- (20) Gmitra, M.; Fabian, J. *Phys. Rev. B: Condens. Matter Mater. Phys.* **2015**, *92*, 155403.
- (21) Qiu, D. Y.; da Jornada, F. H.; Louie, S. G. *Phys. Rev. Lett.* **2013**, *111*, 216805.
- (22) Berkelbach, T. C.; Hybertsen, M. S.; Reichman, D. R. *Phys. Rev. B: Condens. Matter Mater. Phys.* **2013**, *88*, 045318.
- (23) Zhang, C.; Wang, H.; Chan, W.; Manolatu, C.; Rana, F. *Phys. Rev. B: Condens. Matter Mater. Phys.* **2014**, *89*, 205436.
- (24) Li, Y.; Chernikov, A.; Zhang, X.; Rigosi, A.; Hill, H. M.; van der Zande, A. M.; Chenet, D. A.; Shih, E.-M.; Hone, J.; Heinz, T. F. *Phys. Rev. B: Condens. Matter Mater. Phys.* **2014**, *90*, 205422.
- (25) Molina-Sánchez, A.; Palummo, M.; Marini, A.; Wirtz, L. *Phys. Rev. B: Condens. Matter Mater. Phys.* **2016**, *93*, 155435.
- (26) Han, W.; Kawakami, R. K. *Phys. Rev. Lett.* **2011**, *107*, 047207.
- (27) Kioseoglou, G.; Hanbicki, A. T.; Currie, M.; Friedman, A. L.; Jonker, B. T. *Sci. Rep.* **2016**, *6*, 25041.
- (28) Dal Conte, S.; Bottegoni, F.; Pogna, E.; De Fazio, D.; Ambrogio, S.; Bargigia, I.; D'Andrea, C.; Lombardo, A.; Bruna, M.; Ciccacci, F. *Phys. Rev. B: Condens. Matter Mater. Phys.* **2015**, *92*, 235425.
- (29) Sallen, G.; Bouet, L.; Marie, X.; Wang, G.; Zhu, C. R.; Han, W. P.; Lu, Y.; Tan, P. H.; Amand, T.; Liu, B. L.; Urbaszek, B. *Phys. Rev. B: Condens. Matter Mater. Phys.* **2012**, *86*, 081301.
- (30) Zhu, C. R.; Zhang, K.; Glazov, M.; Urbaszek, B.; Amand, T.; Ji, Z. W.; Liu, B. L.; Marie, X. *Phys. Rev. B: Condens. Matter Mater. Phys.* **2014**, *90*, 161302.
- (31) Yang, L.; Sinitsyn, N. A.; Chen, W.; Yuan, J.; Zhang, J.; Lou, J.; Crooker, S. A. *Nat. Phys.* **2015**, *11*, 830–834.
- (32) Bushong, E. J.; Luo, Y. K.; McCreary, K. M.; Newburger, M. J.; Singh, S.; Jonker, B. T.; Kawakami, R. K. *arXiv:1602.03568* 2016.
- (33) Wang, Z.; Ki, D.-K.; Chen, H.; Berger, H.; MacDonald, A. H.; Morpurgo, A. F. *Nat. Commun.* **2015**, *6*, 8339.
- (34) Yang, B.; Tu, M.-F.; Kim, J.; Wu, Y.; Wang, H.; Alicea, J.; Wu, R.; Bockrath, M.; Shi, J. *2D Mater.* **2016**, *3*, 031012.